

Verification Tests for Hybrid Gaussian Beams in Spherical/Time Coordinates

Sean M. Reilly

*Department of Ocean Engineering, University of Rhode Island,
Narragansett RI, USA
campreilly@my.uri.edu*

Gopu Potty

*Department of Ocean Engineering, University of Rhode Island,
Narragansett RI, USA
potty@egr.uri.edu*

Received (Day Month Year)

Revised (10 January 2012)

The previous paper defined a new undersea acoustic propagation loss model that is specifically designed to support real-time, sonar simulation/stimulation systems, in littoral environments, at active sonar frequencies. This paper seeks to verify the model's implementation by comparing the modeled results to analytic solutions.

Keywords: Gaussian beams, 3-D modeling, range-dependent, time-domain.

1. Introduction

The previous paper¹ defined the theory for a new undersea acoustic propagation loss model that is specifically designed to support real-time, sonar simulation/stimulation systems, in littoral environments, at active sonar frequencies. The WaveQ3D model implements this theory using a circular queue of time domain wavefronts, in a fully 3-D ocean environment, with a computationally-efficient form of C++ vector processing.² This follow-up paper analyzes the capabilities and limitations of this implementation. The Capability Maturity Model Integration (CMMI)³ separates testing needed for such an effort into two phases:

- **Verification** testing ensures that selected work products meet their specified requirements. For this analysis, the WaveQ3D model is decomposed into its component parts (such as ray tracing, reflection, eigenray finding, and propagation loss), and the results from each parts are compared to analytic solutions.
- **Validation** testing demonstrates that a product or product component fulfills its intended use when placed in its intended environment. For the WaveQ3D model, this will consist of comparisons to real-world results in a subsequent paper.

Decomposing the testing in this way is designed to ensure that any conclusions drawn from the modeled results rest on a firm foundation of understanding.

2. Ray Tracing Tests

The ray paths in this model use a third order Adams-Bashforth (AB3) marching solution⁴ to create a circular queue of time domain wavefronts. The evolution of the wavefront shape, as it passed through the 3-D ocean environment, is defined by the following equations.

$$\frac{dr}{dt} = c^2 \alpha, \quad (1)$$

$$\frac{d\theta}{dt} = \frac{c^2 \beta}{r}, \quad (2)$$

$$\frac{d\phi}{dt} = \frac{c^2 \gamma}{r \sin \theta}, \quad (3)$$

$$\frac{d\alpha}{dt} = -\frac{1}{c} \frac{dc}{dr} + \frac{c^2}{r} (\beta^2 + \gamma^2), \quad (4)$$

$$\frac{d\beta}{dt} = -\frac{1}{c r} \frac{dc}{d\theta} - \frac{c^2 \alpha \beta}{r} + \gamma^2 \cot \theta, \quad (5)$$

$$\frac{d\gamma}{dt} = -\frac{1}{c r \sin \theta} \frac{dc}{d\phi} - \frac{c^2 \gamma}{r} (\alpha + \beta \cot \theta), \quad (6)$$

where c is the speed of sound as a function of location; t is the travel time; (r, θ, ϕ) are the spherical earth coordinates of the modeled ray path as a function of time; and (α, β, γ) are the spherical earth coordinates of the normalized ray direction as a function of time. The tests discussed in this section analyze the accuracy of Eqs. (1) through (6) in scenarios where the rays do not encounter any boundaries.

2.1. Comparisons to “flat earth” benchmarks

Because WaveQ3D is one of the few models to use non-Cartesian coordinate system, comparisons to other work often require translation before differences can be analyzed. This section analyzes the accuracy of the translation between spherical and Cartesian coordinate models. Cartesian coordinate propagation models frequently use a modified index of refraction⁵ to incorporate earth curvature effects into their calculations.

$$n'(r) = \frac{r}{R} \frac{n(r)}{n(R)}, \quad (7)$$

$$c'(z) = \frac{c(z)}{1 - z/R}, \quad (8)$$

where R is the radius of earth’s curvature in this area of operations; r is the radial distance from the center of curvature (positive is up); $z = R - r$ is the below the ocean surface (positive is down); $n(z), n'(z)$ are the original and modified index of refraction, and $c(z), c'(z)$ are

the original and modified speed of sound. When a testing benchmark is specified in Cartesian coordinate, the inverse of this process must be implemented to create an equivalent environment in spherical earth coordinates.

$$c'(r) = \frac{r}{R} c(r), \quad (9)$$

where $c(r)$ is the benchmark's original $c(z)$ sound speed converted to a function of r .

The Munk profile⁶ was used to evaluate the accuracy of testing Cartesian benchmarks in a model based on spherical earth coordinates. The Munk profile is an idealized representation of a typical deep sound channel, and it was chosen for its ability to support long range paths without interface reflection.

$$z' = 2 \frac{z - z_1}{B}, \quad (10)$$

$$c(z) = c_1 \left[1 + \epsilon \left(z' - 1 + e^{-z'} \right) \right], \quad (11)$$

where z' is the normalized depth (positive is down), z_1 is the depth of the deep sound channel axis (1300 meters), B is a depth scaling factor (1300 meters), c_1 is the sound speed on deep sound channel axis (1500 m/s), and ϵ is the profile scaling factor (7.37×10^{-3}). The specific Munk profile parameters used in this test were selected to match Fig. 3.19 in Jensen, Kuperman, et. al.^{7,8} An example of the ray paths for this profile are illustrated in Fig. 1. This figure was created by WaveQ3D with a 100 ms time increment and 1° separated depression/elevation launch angles from -14° to 14° . Launch angles greater than 14.38° encounter interface reflections.

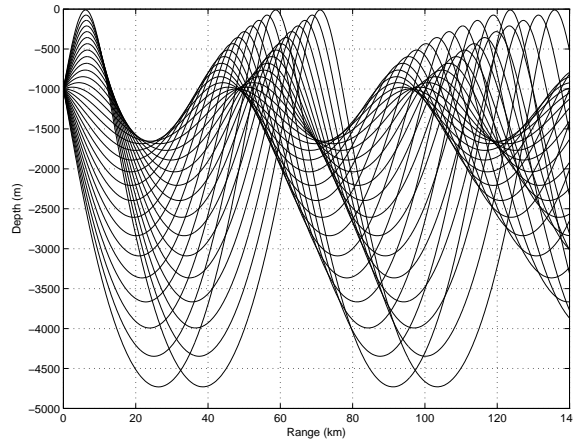


Fig. 1. Modeled ray paths for the Munk profile.

Munk's paper⁶ characterized the analytic solution for ray paths using their cycle range, the range required to complete one period of upward and downward refraction. The cycle

range is equal for positive and negative launch angles. The cycle range was used as the metric for this test because it could be cast into identical units in both spherical and Cartesian coordinates.

To create an analytic equivalent to a typical Cartesian model, Snell's Law (Eq.) was integrated numerically, using the MATLABTM `quadgk()` implementation of an adaptive Gauss-Kronrod quadrature.¹⁰

$$a = \frac{\cos \eta(z)}{c(z)} = \text{constant} , \quad (12)$$

$$\frac{dH}{dz} = \frac{\cos \eta(z)}{\sin \eta(z)} , \quad (13)$$

$$\Delta H = \int_{z_s}^{z_t} \frac{ac(z)}{\sqrt{1 - (ac(z))^2}} dz , \quad (14)$$

$$\Delta t = \int_{z_s}^{z_t} \frac{1}{c(z)\sqrt{1 - (ac(z))^2}} dz , \quad (15)$$

where $\eta(z)$ is the depression/elevation angle along the ray path; a is the ray parameter (constant for each launch angle); H is the horizontal range; t is the travel time; z_s is the source depth; and z_t is the target depth. Although these integrals only apply between the source and the first vertex or reflection, paths out to any range can be constructed by repeating this process after the vertex or reflection.

To create equivalent conditions for a model based on spherical earth coordinates, we modified the original sound speed using Eq. (9), and then performed a similar integration in spherical coordinates. Snell's law in spherical media includes an extra factor of r that is not present in the Cartesian coordinates.⁹ The slope of the ray path also includes an extra factor of r in spherical coordinates.

$$p = \frac{r \cos \eta(r)}{c(r)} = \text{constant} \quad (16)$$

$$\frac{rd\theta}{dr} = \frac{\cos \eta(r)}{\sin \eta(r)} \quad (17)$$

$$\Delta \theta = \int_{r_s}^{r_t} \frac{pc(r)}{r\sqrt{r^2 - (pc(r))^2}} dr \quad (18)$$

$$\Delta t = \int_{r_s}^{r_t} \frac{r}{c(r)\sqrt{r^2 - (pc(r))^2}} dr \quad (19)$$

where $\eta(r)$ is the depression/elevation angle along the ray path; p is the ray parameter for spherical media (constant for each launch angle), $\Delta \theta$ is the horizontal range in solid angle

units; r_s is the radial coordinate for the source depth; and r_t is the radial coordinate for the target depth.

The difference in the cycle ranges computed using these two analytic solutions is shown in 2. The results were computed for two complete periods, with launch angles from 0° to 14° , as a function of the spherical coordinates cycle range solution. The 0° launch angle has difference of -5.14 meters at a range of 96.16 km. The 14° launch angle has a difference of -38.34 meters at range of 129.95 km. The intermediate angles have monotonically increasing values between those two extremes.

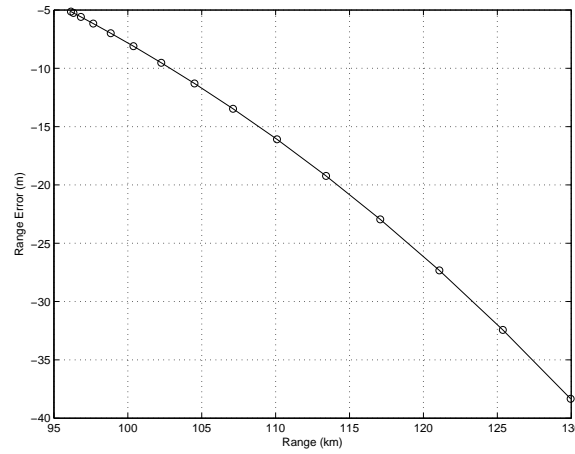


Fig. 2. earth-flattening accuracy for the Munk profile.

Since both solutions are analytic, we conclude that difference must be a fundamental property of ray paths computations in the two coordinate systems. It is equally valid to attribute these results to

- Errors created by a spherical model working with a Cartesian environment, or
- Errors created by a Cartesian model working with a spherical environment.

The second case is more interesting for this study, because it represents a widely accepted (but seldom mentioned) lower limit on ray path range accuracy, approximately 0.03% of the total range.

2.2. Ray path accuracy in a deep sound channel

In this test, the refraction accuracy of the WaveQ3D model was computed for a “flat earth” Munk profile defined in spherical coordinates by combining Eqs. (10) and (11) with Eq. (9). Fig. 3 illustrates the difference between individual WaveQ3D rays and the spherical analytic solution defined by Eqs. (16) through (18). Cycle ranges were computed for both the first and second period of the SOFAR cycle. Because both solutions were computed in spherical

coordinates, using the same sound speed profile, these errors can not be attributed to the use of a modified index of refraction.

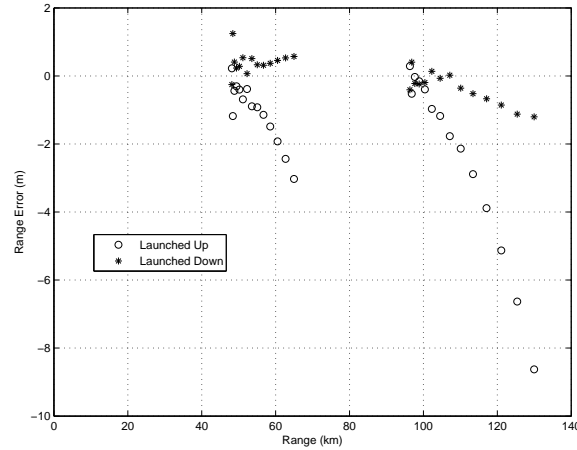


Fig. 3. WaveQ3D errors for the Munk profile.

With a 100 ms step size, the WaveQ3D result deviates from the analytic solution by a maximum of -8.62 meters at cycle range of 129.95 km (0.007% error). However, 50 out of 58 samples (86%) exhibited errors less than ± 2 meters (0.002% error). Ray paths that were initially launched toward the surface, where the sound speed gradient is highest, had consistently larger errors than paths that were launched down. The fact that these errors were all significantly less than those of associated with the earth curvature correction (Fig. 2) suggests that WaveQ3D model's cycle range estimate meets or exceeds the accuracy of Cartesian models used on a spherical earth.

To estimate the impact of WaveQ3D options on this result, the maximum error was also computed as a function of time step size. The circles in Fig. 4 represent maximum errors, across launch angles, for time steps of 25, 50, 100, 150, 200, 250, 300, 350, and 400 ms. The connecting lines smoothly interpolate between these discrete values. From this, we conclude that the accuracy of WaveQ3D cycle range estimates is slightly weaker than a power law; a doubling of the time step decreased the accuracy by approximately a factor of 10. Step sizes as large as 150 yielded results that were at least as accurate as errors associated with the modified index of refraction. Given that some environments may have stronger gradients than the Munk profile, we conclude that a 100 ms step size should be adequate for most long range applications.

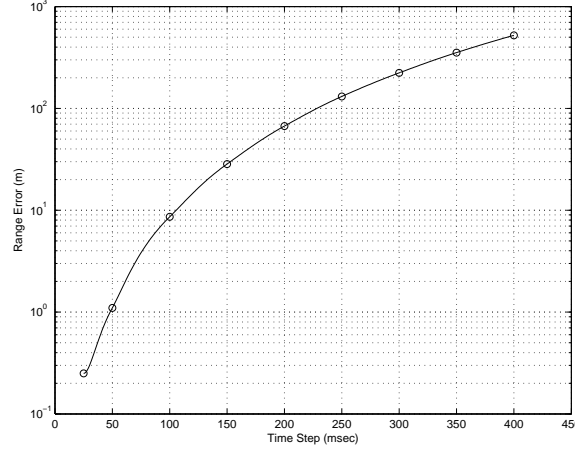


Fig. 4. Path accuracy sensitivity to step size for the Munk profile.

2.3. Ray path accuracy in an extreme downward refraction environment

In this test, the refraction accuracy of the WaveQ3D model was computed for the extreme n^2 linear test case developed by Pedersen and Gordon.¹²

$$c(z) = \frac{c_0}{\sqrt{1 + \frac{2g_0}{c_0}z}} \quad (20)$$

where c_0 is the sound speed at the ocean surface (1550 m/s); g_0 is the sound speed gradient at the ocean surface (1.2 s^{-1}). At shallow depths, this profile matches observed conditions from the Pacific, in an area of extreme velocity gradient. But at depths greater than about 60 meters, it predicts theoretically useful, but physically unrealistic sound speeds. This profile was selected for this study because of its wide use by other authors in the testing of Gaussian beam model behavior at the edge of a shadow zone.^{13,14} (Note that the specific values for this profile parameters were selected to match the MKS representation of Eq. 3.47 in Jensen, Kuperman, et. al.⁷ instead of the English units used in the original Pedersen and Gordon paper.)

The ray paths to be tested for this profile are illustrated in Fig. 5. This figure was created by WaveQ3D with a 100 ms time increment and 1° separated depression/elevation launch angles from 20° to 50° . A “flat earth” adjustment was applied to Eqn. 20 to allow these results to be similar to those computed in Cartesian coordinates. Launch angles greater than 51.21° encounter interface reflections. The rays launched at angles between 44° and 50° travel through a caustic and cross the direct path rays. Because the ray paths were not periodic, we redefined the cycle range as the horizontal range needed to travel up to the first vertex and back to the source depth. Figure 6 illustrates the difference between individual WaveQ3D rays and the spherical analytic solution defined by Eqs. (16) through (18). The WaveQ3D model had a maximum error of 1.3 m at cycle range of 2595.1 m (0.05% error), but there appeared to be a slight bias. We discovered that many of the launch angles had

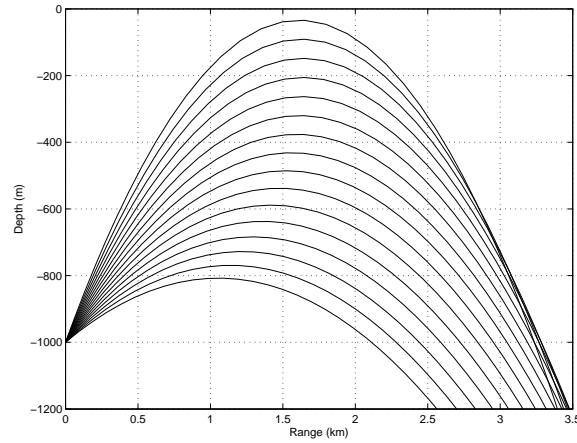
8 *S. M. Reilly, G. Potty*

Fig. 5. Modeled ray paths for the Pedersen/Gordon profile.

cycle range errors right around -0.5 m.

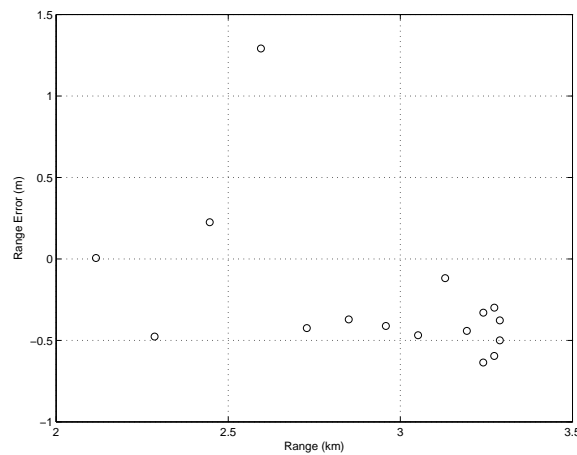


Fig. 6. Path accuracy sensitivity to step size for the Pedersen/Gordon profile.

The sensitivity of these results to time step size is illustrated in Fig. 7. The 150 ms step size had errors of about 2 meters. Errors for smaller time steps approached zero as expected. Larger time steps increase as a power law until the step size was larger than 350 ms, where the error quickly grew to hundreds of meters. This sudden change in error appears to be the result of an inability of model to properly sample the sound velocity profile field at the larger step sizes. From this, we conclude that our earlier 100 ms time step recommendation continues to be valid for this case.

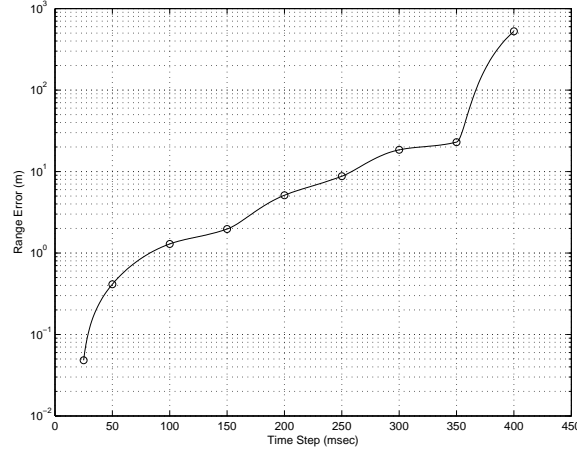


Fig. 7. Ray path accuracy as a function of step size for the Pedersen/Gordon profile.

2.4. Ray path accuracy along great circle routes

In this test, an ocean with a small amount of downward refraction was used to verify the WaveQ3D model's ability to propagate rays along great circle routes. Acoustic rays traveling at a constant depth follow these paths because they are the shortest distance between two points along the earth's surface. The amount of downward refraction needed to parallel the earth's surface was computed by inverting Eq. 9

$$c(r) = \frac{r}{R} c_0. \quad (21)$$

where c_0 was set to 1500 m/s.

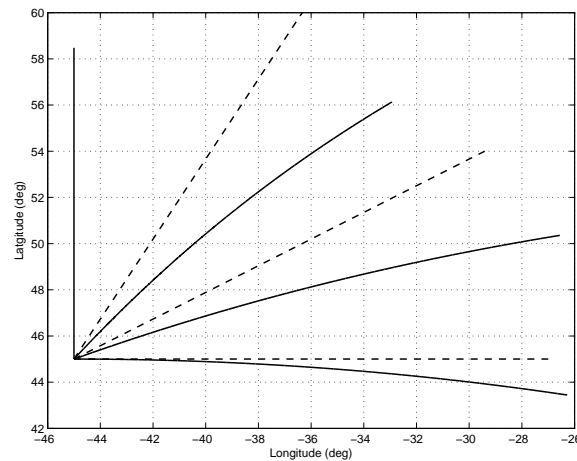


Fig. 8. Great circle routes.

This test launched four horizontal rays from 45N 45W, at a depth of 1000 meters, with azimuths of 0°, 30°, 60°, and 90°. The rays propagated for 1000 s (about 1500 km) with a time step of 100 ms. Fig. 8 illustrates the resulting ray paths as a function of latitude and longitude. The solid lines represent acoustic ray paths while the dashed lines represent the rhumb line paths, paths that would have been taken if latitude/longitude were a Cartesian system. The accuracy of the great circle routes were computed by converting the latitude, longitude, and altitude of each ray back into a great circle azimuth at the point of origin¹¹

$$\varphi_a(t) = \arctan \left[\frac{\cos \chi(t) \sin(\phi(0) - \phi(t))}{\cos \chi(0) \sin \chi(t) - \sin \chi(0) \cos \chi(t) \cos(\phi(0) - \phi(t))} \right], \quad (22)$$

where $\chi(t), \phi(t)$ are latitude and longitude as a function of time; and $\varphi_a(t)$ is the analytic solution for the azimuthal launch angle for a target at $\chi(t), \phi(t)$. The rays traveled at constant depth with a maximum deviation from $\varphi_a(t)$ of 2.81×10^{-10} degrees. This level of accuracy should be more than adequate for most applications.

3. Interface Reflection Tests

The WaveQ3D model estimates the partial time step during a 3-D interface collision using the equation

$$\delta t = \frac{h \hat{r} \cdot \hat{s}}{\frac{d\vec{r}}{dt} \cdot \hat{s}} \quad (23)$$

where \hat{s} is the surface normal; \hat{r} is the unit vector in the radial direction; h is the incident ray height above bottom; δt is the time step needed to reach the interface; and $\frac{d\vec{r}}{dt}$ is the radial ray tracing component defined by Eq. (1). The direction of the 3-D reflection is computed using

$$\hat{R} = \hat{I} - 2(\hat{I} \cdot \hat{s})\hat{s} \quad (24)$$

where \hat{I} is the incident ray path direction; and \hat{R} is the reflected ray path direction. The WaveQ3D model also applies a second order Taylor expansion to each component of the position, normalized direction, and sound speed to improve the accuracy of their values at the time of collision. The tests discussed in this section analyze the accuracy of this reflection process in an isovelocity ocean.

3.1. Reflection accuracy with a flat bottom

This test constructed a geometry in which the changes in latitude and travel time for multiple interface bounces could be calculated analytically. The path of a downwardly steered ray, given a constant bottom depth and latitude change, is illustrated by Fig. 9 and the equations

$$\zeta_s = \arcsin \left(\frac{R^2 - R_b^2 + L^2}{2RL} \right), \quad (25)$$

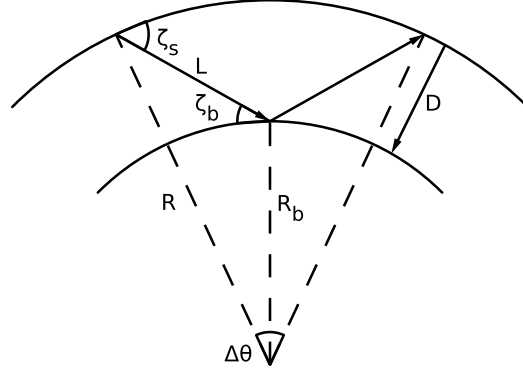


Fig. 9. Flat bottom reflection geometry.

$$\zeta_b = \zeta_s - \Delta\theta/2, \quad (26)$$

$$t = L/c, \quad (27)$$

where R is the radius for the ocean surface; D is the water depth; $R_b = R - D$ is the radius for the ocean bottom; $\Delta\theta$ is the latitude change between surface bounces; L is the path length from surface to bottom; ζ_s is the grazing angle at the surface (also the ray launch angle); ζ_b is the grazing angle at bottom; c is the sound speed; and t is the travel time between the surface and the bottom.

Table 1. Flat bottom expected values.

Parameter	Analytic Result
c	1500 m/s
D	1000 m
$\Delta\theta$	0.2°
ζ_s	5.183617057°
ζ_b	5.083617057°
L	11,175.841460125 m
t	7.450560973 s

$\Delta\theta$ was set 0.2° and the ocean depth was set to 1000 meters, which caused the remaining parameters take on the analytic values shown in Table 1. A single WaveQ3D ray was launched at a depression/elevation angle of -5.183617057° (down), and a time step of 100 ms, which produced the path shown in Fig. 10. After four complete cycles of bottom and surface reflection, a distance of about 89 km, the latitude for the point of reflection deviated from the analytic result by less than 3.9×10^{-7} degrees (about 40 cm). The travel time differed from the analytic result by less than 2.9×10^{-5} s. From this, we conclude that

the WaveQ3D reflection process has an acceptable reflection accuracy when the interfaces are flat.

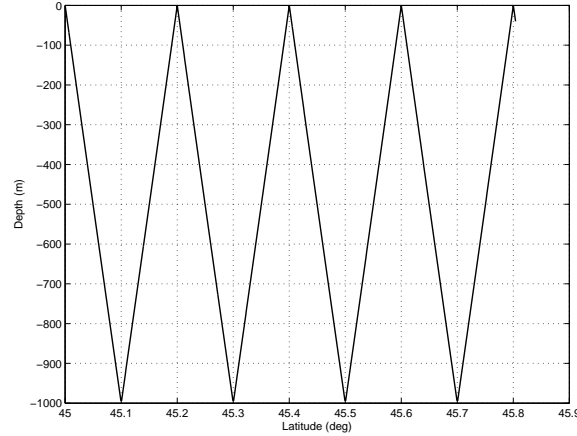


Fig. 10. Flat bottom reflection test results.

3.2. *Reflection accuracy with a sloped bottom*

This test looked at the ability of WaveQ3D to predict the direction of reflection from a bottom that has a 1 degree up-slope in the latitude direction. At each bottom reflection, the depression/elevation angle of the WaveQ3D ray path should decrease by 2° , just like the analytic result. Launching a ray at the same depression/elevation angle as the last test (-5.183617057° , down) produced the results shown in Fig. 11. Note that the time step for this test was set to 1 ms to make it easier to compute depression/elevation angle just before, and just after, each collision. The maximum deviation of any of the three bottom reflections from their analytic reflection direction result was 1×10^{-5} degrees. From this, we conclude that WaveQ3D produces acceptable reflections for sloped bottoms.

3.3. *Out-of-plane reflection from gridded bathymetry*

ETOPO1 gridded bathymetry¹⁵ from the Malta Escarpment was used to qualitatively test out-of-plane reflection from realistic bathymetry features. Out-of-plane reflection is a real-world phenomena that can have a significant impact on shallow water experiments.¹⁶ To isolate the testing to reflection effects, the speed of sound was fixed at 1500 m/s at all locations. WaveQ3D used a 100 ms step size to compute a single path, illustrated in Figure 12. In this figure, bottom bathymetry contours are represented as dashed lines. A ray launched from $35:59\text{N } 16:00\text{E}$, at a depth of 10 meters, with a depression/elevation angle of -20° (down), and an azimuth of 270° traveled along the path illustrated by the solid black line. The closed circles along this path represent places where bottom reflections occurred;

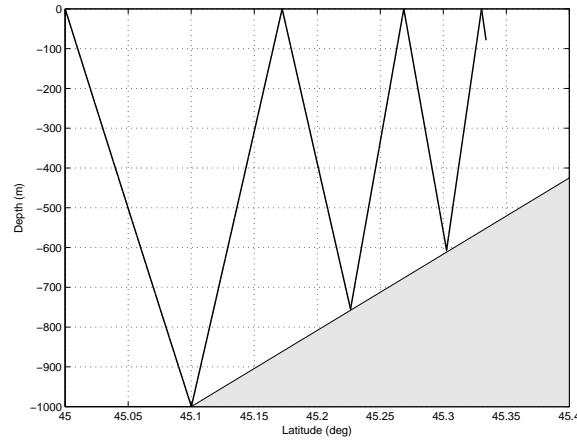


Fig. 11. Analytic slope reflection test results.

the open circles represent surface reflections. The decrease in spacing between the shallow water dots illustrates the type of depression/elevation angle change (Fig. 11) expected for sloped bottoms. What was new in this test was the fact that ray paths were reflected into a new azimuthal direction each time that they interacted with the bottom. These out-of-plane reflections resulted in a down slope ray path that was offset by more than 21.9 km from the up slope path, after 14 bounces off of the bottom. From this, we conclude that WaveQ3D results will have a significant contributions from out-of-plane ray paths whenever there are multiple interactions with complex bottom bathymetry features.

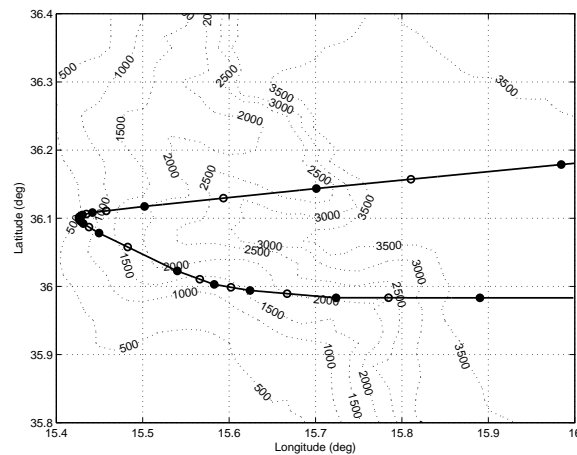


Fig. 12. Reflection on the Malta Escarpment.

4. Eigenray and Propagation Loss Tests

The tests discussed in this section compare WaveQ3D's eigenray and propagation loss calculation to analytic solutions.

The WaveQ3D eigenray estimation process establishes the relative geometry between rays paths and targets. That geometry then allows the calculation of travel time (t), source angle (μ), and target angle (φ) for each multi-path arrival. WaveQ3D computes these eigenray products by searching for the offsets which minimize the squared distance from targets to points on the wavefront. Once the CPA has been determined, the 3-D offset to the target is computed using

$$\vec{\rho} \equiv (\rho_1, \rho_2, \rho_3) \equiv (\delta t, \delta \mu, \delta \varphi) , \quad (28)$$

$$\vec{g} \equiv \frac{\partial d^2}{\partial \vec{\rho}} \Big|_{CPA} , \quad (29)$$

$$\mathbf{H} \equiv \frac{\partial^2 d^2}{\partial \vec{\rho}^2} \Big|_{CPA} \quad (30)$$

$$\vec{\rho} = -\mathbf{H}^{-1} \vec{g} . \quad (31)$$

where $\vec{\rho}$ is the offset from CPA in vector form; d^2 is the squared distance from each point on the wavefront to the target; \vec{g} is the gradient of squared distance, evaluated at CPA (3 elements), and \mathbf{H} is the Hessian matrix of squared distance, evaluated at CPA (3x3).

The propagation loss at the target location is a summation of contributions from the rays that surround the eigenray target. To create a 3-D acoustic field across the wavefront, WaveQ3D uses independent Gaussian beams in the μ and φ directions and ignores the cross terms.

$$G(\vec{r}_p) = \left(\sum_{j'=j-J}^{j+J} g_{j'}(\vec{r}_p) \right) \left(\sum_{k'=k-K}^{k+K} g_{k'}(\vec{r}_p) \right) , \quad (32)$$

$$g_{j'}(\vec{r}_p) = \frac{(\mu_{j'+1} - \mu_{j'})}{\sqrt{2\pi w_{j'}^2}} \exp \left(-\frac{d_{j'}^2}{2w_{j'}^2} \right) , \quad (33)$$

$$g_{k'}(\vec{r}_p) = \frac{(\sin(\mu_{j'+1}) - \sin(\mu_{j'})) (\varphi_{k'+1} - \varphi_{k'})}{\sqrt{2\pi w_{k'}^2}} \exp \left(-\frac{d_{k'}^2}{2w_{k'}^2} \right) , \quad (34)$$

where $G(\vec{r}_p)$ is the total Gaussian beam intensity at the eigenray target; (j, k) are the index numbers of wavefront cell containing the eigenray target; $g_{j'}$ are the Gaussian beam contributions along depression/elevation direction; $g_{k'}$ are the Gaussian beam contributions

along the azimuthal direction; $2J + 1$ are the number of significant beams in the depression/elevation direction; and $2K + 1$ are the number of significant beams in the azimuthal direction; w_j and w_k are the half-widths of the Gaussian beam in the μ and φ directions; and d_j^2 and d_k^2 are the distance in the μ and φ directions from the Gaussian beam center to the eigenray target. The WaveQ3D implementation divides the wavefront into ray families based on the number of surface reflections, bottom reflections, and caustic encounters. Within each ray family, propagation loss contributions are added across the wavefront until an edge is hit or the accumulated loss result changes by less than 0.01 dB.

WaveQ3D treats the beam width calculation as a convolution between Weinberg's frequency dependent "minimum width" term¹⁴ and a second Gaussian that represents the spatial spreading created by the sampling of the wavefront.

$$(w'_{j,k}(f))^2 = (2w_{j,k})^2 + (2\pi\lambda)^2 . \quad (35)$$

where λ is the wavelength of the signal being modeled; $w_{j,k}$ is the cell width of beam j or k , and $w'_{j,k}(f)$ is the adjusted width of beam j or k . The factor of 2 in the $w_{j,k}$ term creates a minimum overlap of 50% between neighboring beams. Normalizing Eqs. (33) and (34) by the combined effect of both spreading sources conserves energy across the wavefront.

4.1. Eigenray accuracy for a simple geometry

This test constructs a short range geometry in which travel time, source angle, and target angle can be computed analytically for direct path, surface reflected, and bottom reflected paths on a spherical earth. The geometry for this test is illustrated in Fig. 13.

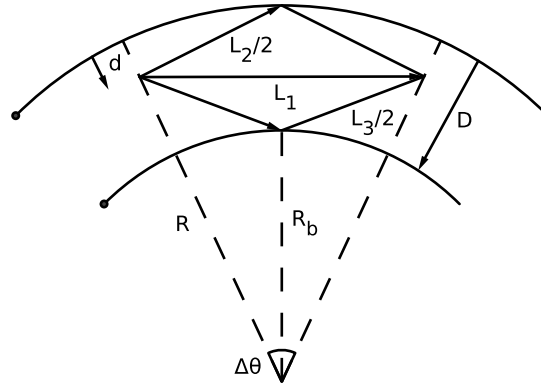


Fig. 13. Flat bottom eigenray test geometry.

$$r = R - d , \quad (36)$$

$$L_1 = 2r \sin(\Delta\theta/2) , \quad (37)$$

$$\mu_1 = 90^\circ - \arccos\left(\frac{L_1}{2r}\right), \quad (38)$$

$$L_2 = 2\sqrt{(L_1/2)^2 + [R - r \cos(\Delta\theta/2)]^2}, \quad (39)$$

$$\mu_2 = 90^\circ - \arccos\left(\frac{d}{L_2/2}\right), \quad (40)$$

$$L_3 = 2\sqrt{(L_1/2)^2 + [r \cos(\Delta\theta/2) - (R - D)]^2}, \quad (41)$$

$$\mu_3 = \mu_1 + \arccos\left(\frac{L_1/2}{L_3/2}\right), \quad (42)$$

$$t_n = L_n/c, \quad (43)$$

where c is the sound speed; D is the water depth; d is both the source and target depth; r is the distance of the source/target from the center of curvature; L_1, L_2, L_3 are the path lengths for the direct, surface reflected, and bottom reflected paths; t_1, t_2, t_3 are the travel times; and μ_1, μ_2, μ_3 are the source/target depression/elevation angles.

WaveQ3D was tested using an ocean depth of 3000 m, a $\Delta\theta$ value of 0.02° , and the source/target depth of 1000 m. Eqs. (36) through (43) were then used to compute the values shown in Table 2.

Table 2. Expected eigenray values for a simple geometry.

Parameter	Analytic Result
D	3000 m
d	1000 m
$\Delta\theta$	0.02°
t_1	1.484019 s
t_2	1.995103 s
t_3	3.051677 s
μ_1	-0.010000°
μ_2	41.936232°
μ_3	-60.912572°

WaveQ3D eigenrays were calculated using a ray fan with depression/elevation angles from -60° to $+60^\circ$, azimuth angles from -4° to $+4^\circ$, angle spacings of 1° in both directions, and a time step of 100 ms. This geometry was specifically designed to stress the model by forcing it to extrapolate the bottom bounce path from a location outside of the ray fan. The other two paths are firmly inside of the ray fan.

For the direct path, the maximum difference between the modeled times/angles and their analytic counterparts were 2.2×10^{-5} ms and 1.1×10^{-4} degrees. These values represented

eigenray accuracy limitations purely derived from Eqs. (28) through (31). The equivalent measurements for the surface reflected path yielded differences of 2.2×10^{-3} ms and 4.8×10^{-3} degrees. The reduced accuracy of the surface reflected paths appears to be due to limitations in the interface reflection process. Even though the bottom reflected path was extrapolated from outside of the ray fan, it still achieved accuracies of 1.7 ms and 0.91° . We believe that any of these eigenray accuracies should be adequate for most sim/stim applications.

4.2. Eigenray accuracy for Lloyd's mirror on spherical earth

On a flat earth, the Lloyd's mirror geometry generates exactly two paths: a direct path and a surface reflection. However (as shown in Fig. 14) isovelocity ray paths actually form unexpected caustics when the curvature of the earth is incorporated. Fig. 15 illustrates that these caustics are formed by focusing from the concave surface of the earth. Incorporating these effects into our eigenray tests is important because of WaveQ3D's use of spherical earth coordinates.

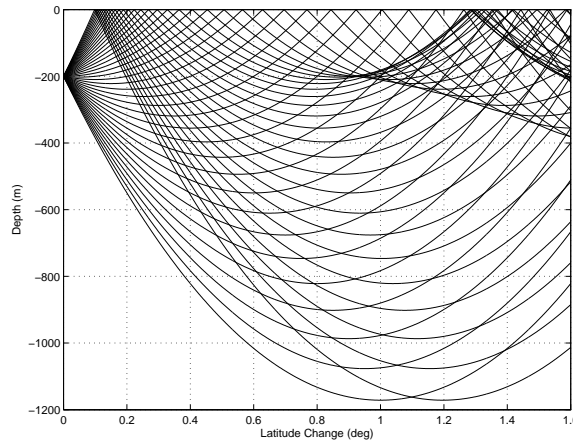


Fig. 14. Isovelocity paths in spherical coordinates.

Fig. 16 defines the geometry used to compute an analytic eigenray solution. In this figure, d_1, d_2 are the source and target depths; r_1, r_2 are the source and target distance from the center of curvature; $\Delta\theta$ is the latitude change from source to target; $\Delta\theta_1$ is the latitude change from the source to the point of reflection; $\Delta\theta_2 = \Delta\theta - \Delta\theta_1$ is the latitude change from the reflection point to the target; β is the reflection angle relative to the normal; a is the length of the direct path; and $b_1 + b_2$ is the length of the surface reflected path.

The analytic solutions for the surface reflected path requires finding values of $\Delta\theta_1$ which solve the transcendental equation (derived in the Appendix A)

$$r_1 \sin(\Delta\theta_1) - r_2 \sin(\Delta\theta - \Delta\theta_1) + \frac{r_1 r_2}{R} \sin(\Delta\theta - 2\Delta\theta_1) = 0. \quad (44)$$

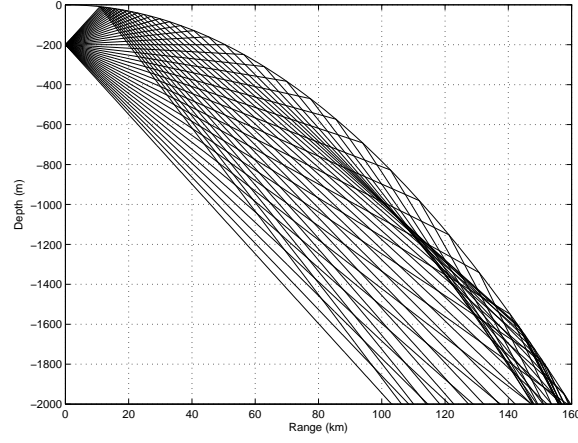


Fig. 15. IsovLOCITY paths in Cartesian coordinates.

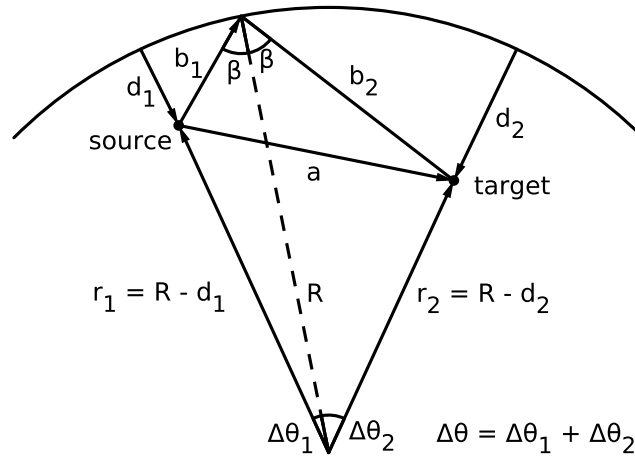


Fig. 16. Ocean surface as concave reflector.

Once the roots of Eq. (44) are known, the analytic solution for surface reflected eigenrays can be computed using

$$b_1^2 = R^2 + r_1^2 - 2Rr_1 \cos(\Delta\theta_1), \quad (45)$$

$$b_2^2 = R^2 + r_2^2 - 2Rr_2 \cos(\Delta\theta_2), \quad (46)$$

$$t_s = \frac{b_1 + b_2}{c_0}, \quad (47)$$

$$\mu_{s,source} = -\arcsin\left(\frac{b_1^2 + r_1^2 - R^2}{2b_1r_1}\right), \quad (48)$$

$$\mu_{s,target} = \arcsin\left(\frac{b_2^2 + r_2^2 - R^2}{2b_2r_2}\right), \quad (49)$$

where t_s is the surface-reflected travel time from source to target; $\mu_{s,source}$ is the surface-reflected depression/elevation angle at source; and $\mu_{s,target}$ is the surface-reflected depression/elevation angle at target.

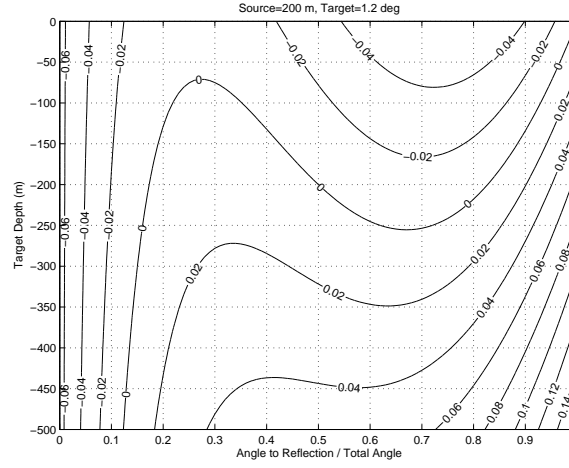


Fig. 17. Roots of surface reflection transcendental equation.

Fig. 17 illustrates the roots of Eq. (44) for a source depth of 200 meters. The horizontal axis is the ratio of $\Delta\theta_1/\Delta\theta$. The vertical axis defines target depths from 0 to 500 meters. The contours on this plot represent the values for the left hand side of Eq. (44), multiplied by 10^5 , for a target $\Delta\theta$ of 1.2° . The zero contour illustrates the location of the roots at each target depth. For example, we found that there are three roots for $\Delta\theta_1$ at values of $\Delta\theta$ times 0.190047203712437, 0.425088688451783, and 0.88486312787168 when a target depth was 150 meters. The physical interpretation of the multiple roots is that there are multiple surface-reflection paths focused onto the target location by the concave surface of the earth.

Table 3. Expected eigenray values for target at 1.2° and 150 m.

Path	Travel time	Launch angle	Target angle
Direct Path	89.05102557 s	-0.578554378°	+0.621445622°
Surface 1	89.05369537 s	+0.337347599°	+0.406539112°
Surface 2	89.05379297 s	-0.053251329°	+0.233038477°
Surface 3	89.05320459 s	-0.433973977°	-0.48969753°

The analytic eigenray products for a target at a depth of 150 m are shown in Table 3. WaveQ3D was run with a time step of 100 ms and a depression/elevation launch angle spacing of 0.05° . The travel times computed by WaveQ3D matched the analytic result to within 1.2×10^{-5} s, and the angles were accurate to within 0.012° . Note that the launch angle spacing was much tighter than other tests because WaveQ3D's eigenray searching logic is limited to finding one ray path between any two launch angles. A larger launch angle increment in this test would have caused the model to fail to find the "Surface 3" path. But with this context, we felt that WaveQ3D was quite accurate in predicting the travel times and angles for the equivalent of a Lloyd's mirror geometry on a spherical earth.

4.3. Eigenray robustness for Lloyd's mirror on spherical earth

This test extends the results of the previous section by comparing modeled travel times and ray path angles, for the spherical equivalent of Lloyd's mirror, at a variety of depths and ranges. This test used a isovelocity speed of sound of 1500 m/s, a frequency of 2000 Hz, a source depth of 200 m, target depths from 0 to 1000 m, 181 tangent spaced depression/elevation angles (explained in the Appendix B), 1° spaced azimuth angles from -4° to $+4^\circ$, and a time step of 100 ms. The maximum range was limited to $\Delta\theta = 0.8^\circ$ to ensure that only a single surface reflected path was produced at each target location (see Fig. 14). This choice allows the test to be run with a ray spacing that was much more typical than the fine scale D/E angles used in the previous section.

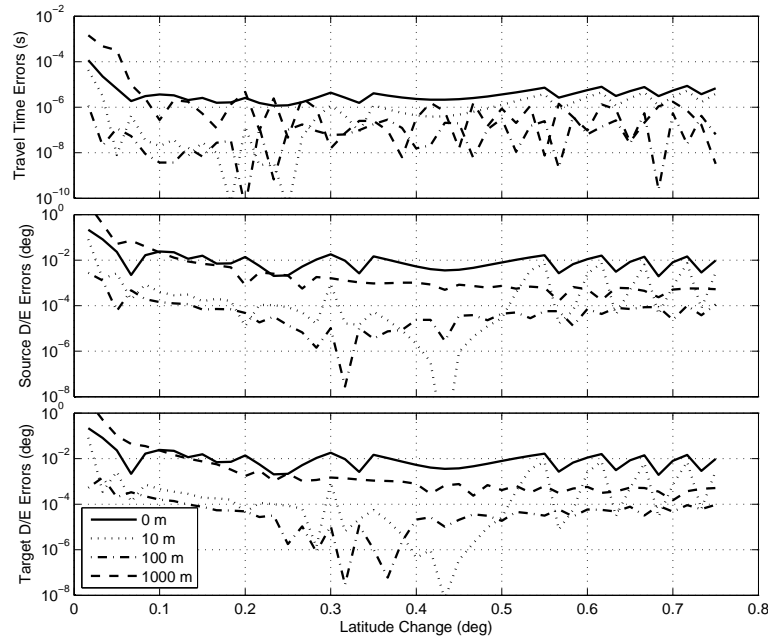


Fig. 18. Eigenray errors for Lloyd's mirror direct path.

The eigenray errors for direct path are summarized in Fig. 18. Each plot shows the absolute value of the difference between the WaveQ3D model and the analytic solution, as a function of range, for targets at depths of 0, 10, 100, and 1000 m. Beyond a range of 0.1° (about 11 km), the direct path model had maximum errors in travel time error and angle of 0.0087 ms and 0.024° . In each case, these errors were larger at short ranges. The short range errors were most pronounced near the ocean surface and at the 1000 m depth.

The eigenray errors for the surface reflected path are shown in Fig. 19. Once again, the errors were largest at short ranges, both near the ocean surface and at the 1000 m depth. Beyond a range of 0.1° , the surface reflected path model has a maximum travel time error of 0.0041 ms, a maximum source angle error of 0.055° and a maximum target angle error of 0.047° . In each case, the errors are larger at short ranges.

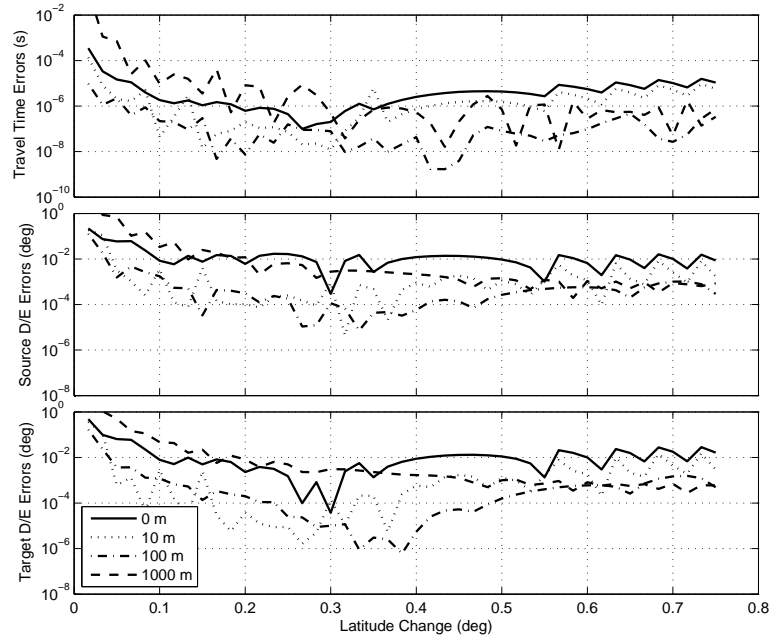


Fig. 19. Eigenray errors for Lloyd's mirror surface reflected path.

The inaccuracies near the surface were attributed to undersampling by the 100 ms time step, as illustrated in Fig. 20. The solid lines in this figure represent direct path rays that are moving out in range and up toward the surface from the source at 200 m. The dashed lines present the same ray paths after reflection from the ocean surface. The dotted lines that connect them represent discontinuities between the direct path and surface reflected segments of the wavefront. At short ranges, these discontinuities cause the edges of ray families to be far from targets that are near the interface; extrapolation led to inaccuracy. Shortening the time step mitigates this source of inaccuracy. At longer ranges, this source of inaccuracy is automatically reduced by the fact that the edges of the ray families get

22 *S. M. Reilly, G. Potty*

closer to the surface as the rays become more horizontal.

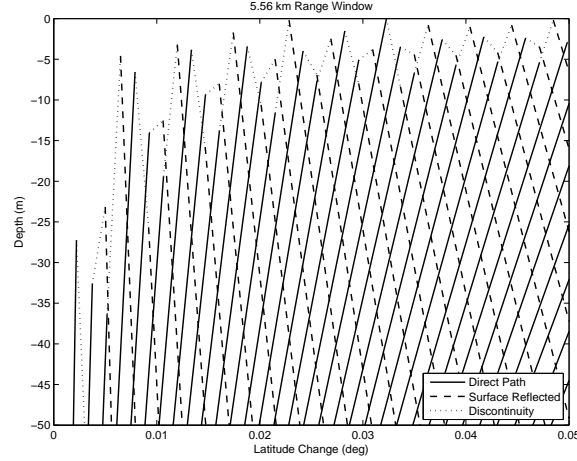


Fig. 20. Time-step effects near the ocean surface.

The errors at large depths were attributed to the tangent spaced depression/elevation angles used in this test. Using a more uniform scheme for depression/elevation angles would have mitigated this source of inaccuracy.

4.4. Propagation loss accuracy for Lloyd's Mirror

Near the surface, WaveQ3D must extrapolate eigenrays from distances that are up to 1.5 paths away from the interface. The tests in this section were designed to expose the impact of this limitations on propagation loss accuracy. The analytic solutions for these test were derived in Cartesian coordinates using the method of images.

$$p(r, z) = \frac{e^{ikL_1}}{L_1} - \frac{e^{ikL_2}}{L_2}; \quad (50)$$

$$L_1 = \sqrt{r^2 + (z - z_s)^2}; \quad (51)$$

$$L_2 = \sqrt{r^2 + (z + z_s)^2}; \quad (52)$$

where r is the target range; z is the target depth (positive is down); z_s is the source depth (positive is down); L_1 is the slant range to source; L_2 is the slant range to image source (above water); k is the acoustic wave number ($2\pi f/c$); and f is the signal frequency; c is the speed of sound; $p(r, z)$ is the complex pressure.

The propagation loss for a 200 meters deep target is shown as a function of range in Fig. 21 and Fig. 22. Results for a 10 km range target are shown as a function of depth in Fig. 23. Both cases used a speed of sound of 1500 m/s, with a “flat earth” adjustment

from Eq. (9), a frequency of 2000 Hz, a source depth of 75 m, 181 tangent spaced depression/elevation angles, 1° spaced azimuth angles from -4° to $+4^\circ$, and a time step of 100 ms. Figure 22 highlights fact that the errors in Fig. 21 are most severe at range less than 2 km. Figure 22 illustrates that fact that the largest errors, as a function of depth, are right below the ocean surface. We attribute the ocean surface results to small in the computation of travel time for the direct and surface reflected paths.

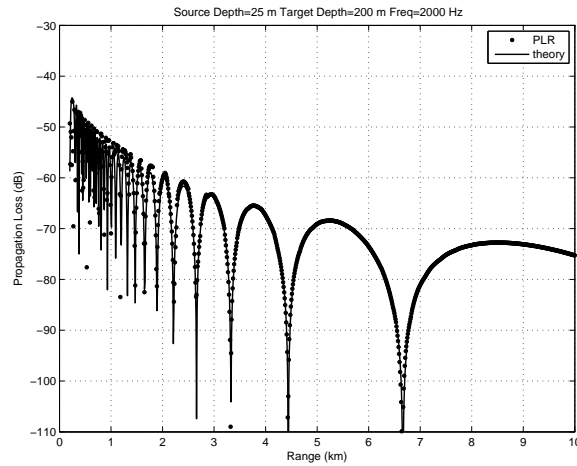


Fig. 21. Lloyd's mirror propagation loss as a function of range.

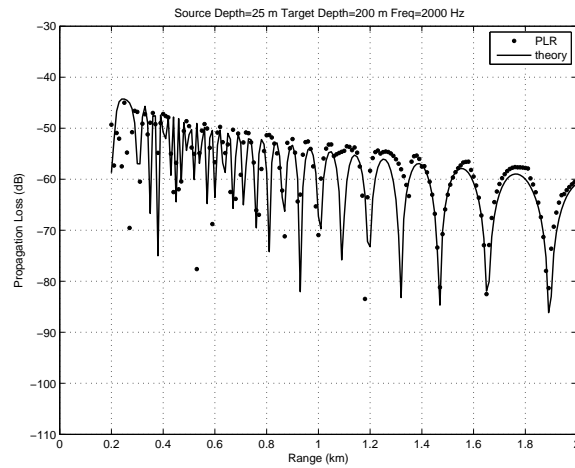


Fig. 22. Lloyd's mirror propagation loss errors at short ranges.

To compare these results quantitatively, we will use a set of statistical measures that are defined in detail in Appendix C. The differences between the WaveQ3D model and

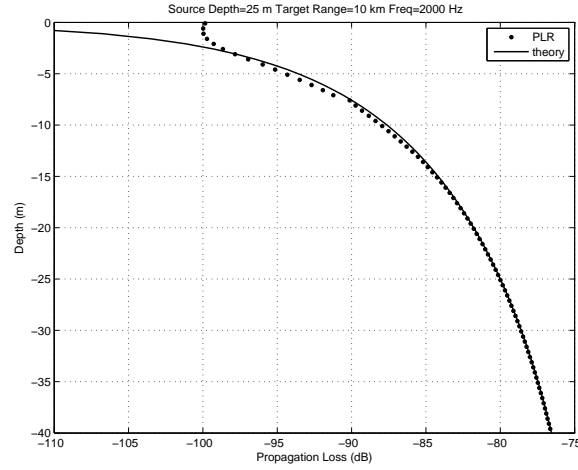


Fig. 23. Lloyd's mirror propagation loss as a function of depth.

the analytic results are summarized in Table 4. From this, we conclude that, although the WaveQ3D model's Lloyd's Mirror predictions clearly has limitations, those limitations will have a limited impact on its ability to accurately model propagation loss in a Lloyd's mirror environment.

Table 4. Lloyd's Mirror propagation loss accuracy.

Scenario	bias	deviation	r^2
Lloyd's Mirror vs. range	+0.42 dB	± 3.51 dB	87.2%
Lloyd's Mirror vs. depth	+0.50 dB	± 3.45 dB	87.2%

4.5. *Eigeneray and propagation loss accuracy in an extreme downward refraction environment*

In this test, the eigeneray and propagation loss accuracy of the WaveQ3D model were analyzed for the extreme n^2 linear test case developed by Pedersen and Gordon.¹² Two geometries were supported in this test:

- The shallow source geometry puts the source at a depth of 75 m and creates a series of targets at a depth of 75 m with ranges from 500-1000 m.
- The deep source geometry puts the source at a depth of 1000 m and creates a series of targets at a depth of 800 m with ranges from 3000-3100 m.

Both cases used the profile defined in Eq. (20), with a “flat earth” correction using Eq. (9), and a frequency of 2000 Hz. The eigenrays for the WaveQ3D model were compared to both the GRAB model¹⁷ and analytic solutions. The comparison to GRAB, a U.S. Navy

standard, was included to assess WaveQ3D error statistics against a well understood, high quality, Gaussian beam model.

Shallow source geometry

Figure 24 is a ray trace for the shallow source geometry. This plot illustrates a ray fan with launch angles from 0° to 25° in 0.5° increments. The target locations are illustrated by the horizontal black line. There are two potential eigenrays for each target. The direct path and surface reflected components of the wavefront at 0.4 sec are illustrated with circle and square symbols. Rays launched below the critical angle (18.82°) form the direct path contribution after traveling through an upper vertex. (Because this geometry does not support the formation of a caustic, neither WaveQ3D nor GRAB applies a $-\pi/2$ phase shift to this path.) Rays above the critical angle hit the surface before ensonifying the target. Both ray families included targets that were ensonified in their evanescent region, the region outside of the ray fan.

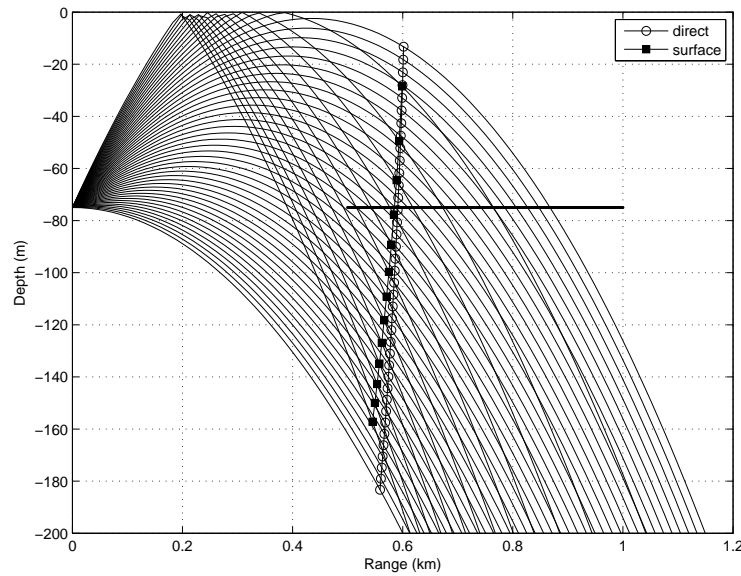


Fig. 24. Ray trace for shallow source.

Figures 25 and 26 compare the individual WaveQ3D and GRAB eigenrays for the direct and surface reflected paths. Analytic solutions for the travel time and rays angles were also computed using Eqn. (16) through (19). To highlight differences in travel time, a bulk time has been removed using the slope of the analytic solution for the direct path.

The GRAB model was configured using ray fan with launch angles from 0° to 25° in 0.1° increments. However, it is important to note that, using the sound speed at the source,

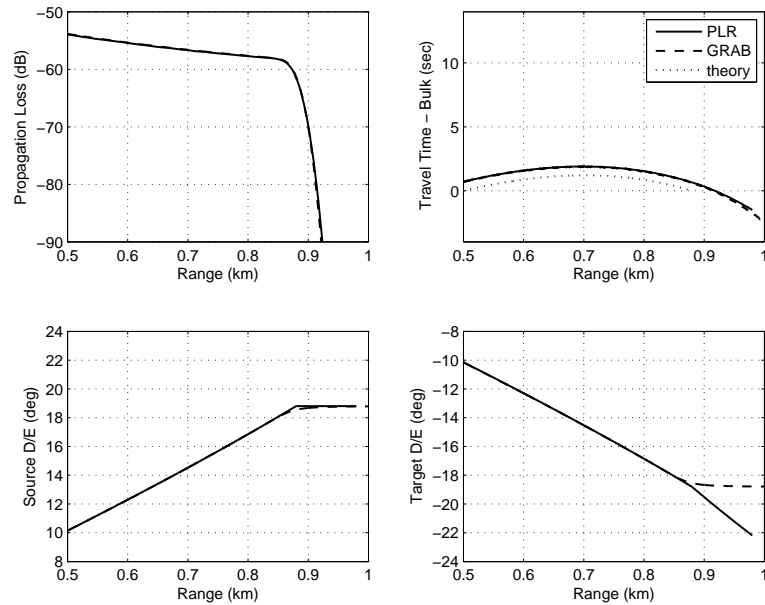


Fig. 25. Direct path eigenrays for shallow source.

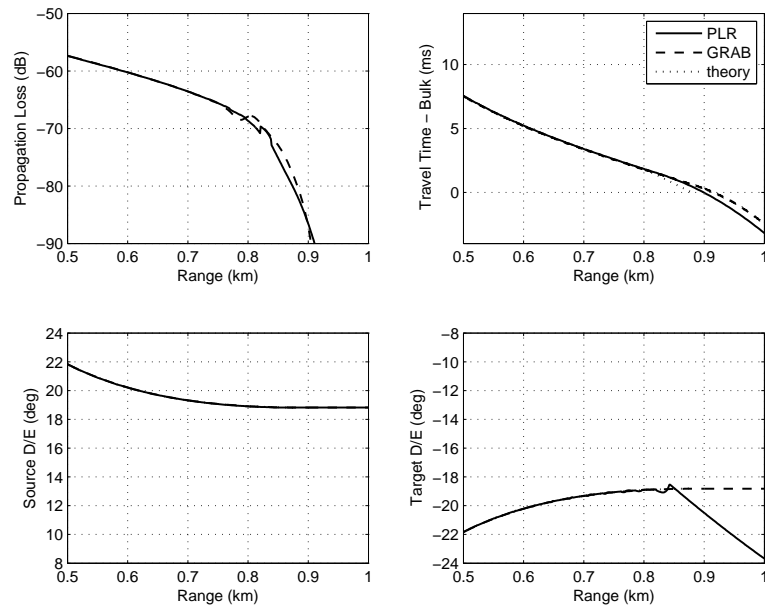


Fig. 26. Surface reflected eigenrays for shallow source.

GRAB automatically enhances the fan around the critical with 11 additional beams with spacings of 0° , $\pm 0.03125^\circ$, $\pm 0.0625^\circ$, $\pm 0.125^\circ$, $\pm 0.25^\circ$, and $\pm 0.5^\circ$. If these small rays spacings

were not used near the critical ray, it would lead to un-realistically large gaps between the outer edge of each ray family and the critical ray. This is especially true for the surface reflected path in this geometry.

To achieve a similar effect, WaveQ3D was configured with 0.025° spaced depression/elevation angles from 0° to $+25^\circ$ and 1° spaced azimuth angles from -4° to $+4^\circ$. Because this geometry evolves so quickly in time, the WaveQ3D results were created using a 10 ms time step instead of the 100 ms value used in other tests.

Table 5. Individual eigenrays for shallow source.

Scenario	bias	deviation	r^2	time	source DE	target DE
GRAB Direct	-	-	-	0.74 ms	0.25°	0.25°
GRAB Surface	-	-	-	0.66 ms	0.02°	0.02°
WaveQ3D Direct	+0.03 dB	± 0.46 dB	99.9%	0.71 ms	0.00°	0.00°
WaveQ3D Surface	0.00 dB	± 1.40 dB	99.1%	0.47 ms	0.02°	0.99°

Quantitative results for the shallow source's individual eigenrays are summarized in Table 5. In this table, the maximum difference in travel time, source depression/elevation angle, and target depression/elevation angle are computed relative to the analytic solution. Those time and angle comparisons are limited to non-evanescent regions, where the analytic solutions had real values. Because our analytic solution did not support propagation loss for individual eigenrays, WaveQ3D values were compared to GRAB in this table.

From these results, we conclude that GRAB and WaveQ3D have similar eigenray accuracy when compared to analytic solutions. In this case, the major difference appears to be differences in the way that GRAB and WaveQ3D handle depression/elevation angles near the shadow zone. GRAB's angles are a weighted sum of contribution from neighboring Gaussian beams. This gives GRAB a smooth roll-off from angles inside the ray fan to a constant value on the outside. GRAB's constant value is taken from the closest ray in horizontal range. In contrast, the WaveQ3D angles are computed from the geometry of eigenray offsets. Outside of the ray fan, WaveQ3D uses angles from the ray that is closest in slant range. Because the rays in this geometry are rapidly changing direction near the shadow zone, the difference between slant and horizontal range results in WaveQ3D target depression/elevation angles that are up to 4° different than the GRAB result. But because the analytic solution is not valid in this region, that difference is not reflected in Table 5.

Differences in total propagation loss for the shallow source geometry are illustrated in Fig. 27 and summarized in Table 6. The analytic solution for this test were computing using the Fast Field Program (FFP) wavenumber integration technique.^{18,19} Note that, in all regions, this implementation of FFP was consistent with an ideal wave equation solution, except for the presence of some implementation jitter in the ranges above 880 m. In the region between 500-750 m, all three models produced almost identical results. As target passed into the shadow zone region, WaveQ3D and GRAB produced values that were similar to each other, but slightly higher than FFP. But we also noted that, if a coarser set of

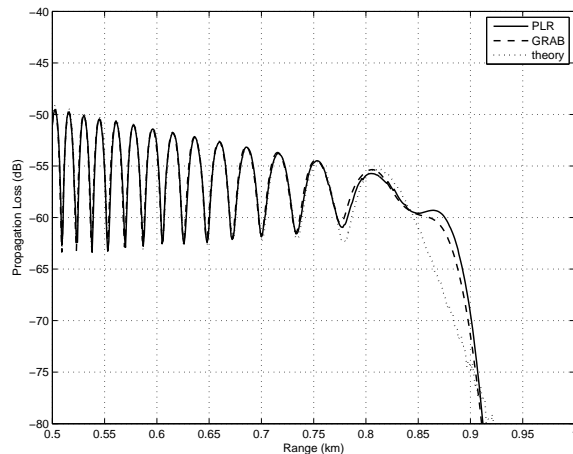


Fig. 27. Propagation loss for shallow source.

depression elevation launch angles was used for WaveQ3D, the surface reflected path would have disappeared prematurely, which would have manifested as shadow zone oscillations in the total propagation loss. Taken as a whole, we feel confident that Wave3D propagation loss errors are similar to those of GRAB for this scenario.

Table 6. Total propagation loss for shallow source.

Scenario	bias	deviation	r^2
GRAB	+0.71 dB	± 1.78 dB	92.5%
WaveQ3D	+0.80 dB	± 2.21 dB	88.7%
GRAB ≤ 0.75 km	+0.09 dB	± 0.58 dB	97.7%
WaveQ3D ≤ 0.75 km	-0.03 dB	± 0.47 dB	98.4%

Deep source geometry

Figure 28 is a ray trace for the deep source geometry. This plot illustrates a ray fan with launch angles from 20° to 60° in 1° increments. The target locations are illustrated by the horizontal black line. There are three potential eigenrays for each target. Rays launched above the critical angle (51.21°) hit the surface before ensonifying the target. However, because all of the surface reflected paths are far from the targets, their contribution to the overall solution is weak. Starting at around 2.5 seconds of travel time, the outer edge of the wavefront folds back on itself and splits the remaining contributions into strong direct path and caustic ray families. The direct path, surface reflected, and caustic components of the wavefront at 2.5 sec are illustrated with circle, square, and diamond symbols on Fig. 28.

Figures 29 and 30 compare the individual WaveQ3D and GRAB eigenrays for the deep source's direct and caustic paths. As before, a bulk time has been removed using the slope of

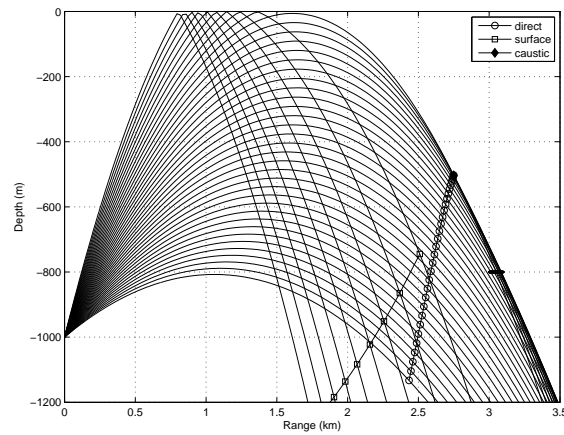


Fig. 28. Ray trace for shallow source.

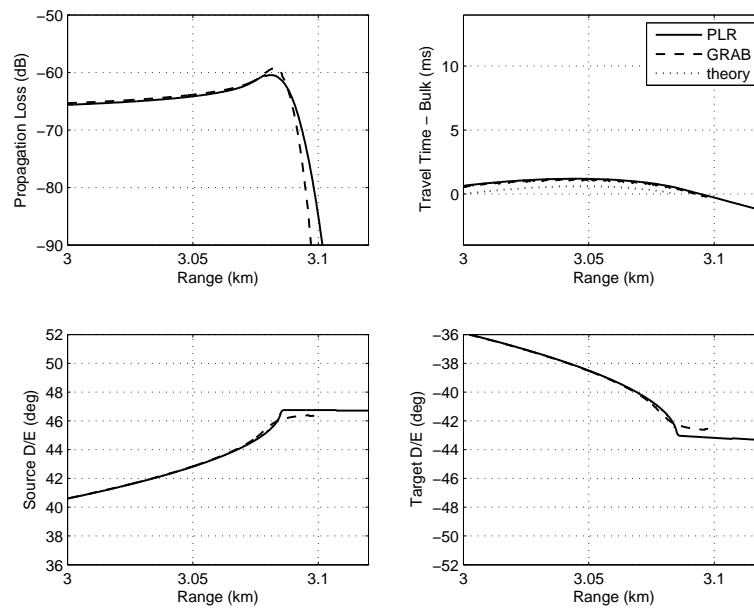


Fig. 29. Caustic eigenrays for deep source.

the analytic solution for the direct path. In these results, the GRAB model was configured using ray fan with launch angles from 20° to 60° in 0.1° increments and rays near the caustic were automatically augmented. WaveQ3D used a ray spacing of 0.25° spacing to achieve a similar result.

The big difference between the models appears to be the fact that the WaveQ3D transmission loss has a more gradual roll-off into the shadow zones than GRAB. Quantitative

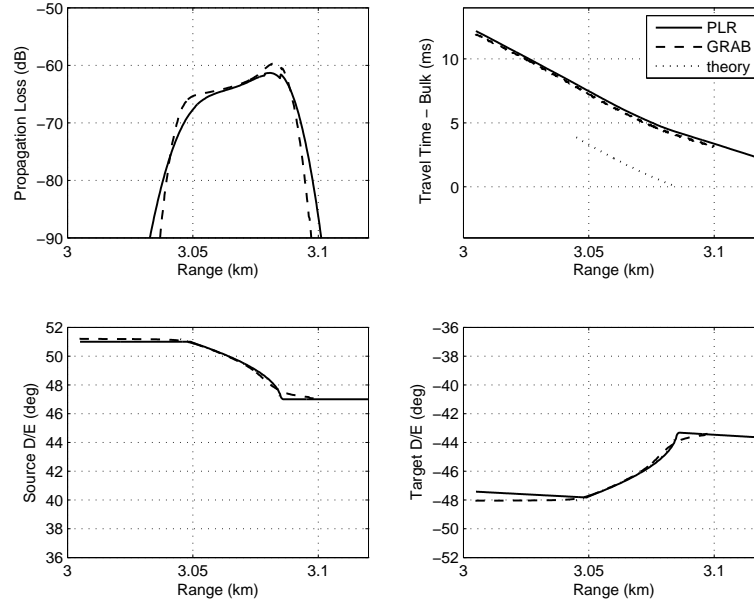


Fig. 30. Direct path eigenrays for deep source.

comparisons for the deep source's individual eigenrays are summarized in Table 7. The statistics for the WaveQ3D angles for the caustic path are skewed by the fact that differences in launch angle resolutions causes inner edge of the WaveQ3D result to prematurely transition to its shadow zone result. In other regions, the agreement is much closer. It is also important to note that the depression/elevation angle deviations seen in the WaveQ3D results for the shallow source are less evident in the deep source case.

Table 7. Individual eigenrays for deep source.

Scenario	bias	deviation	r^2	time	source DE	target DE
GRAB Direct	-	-	-	0.65 ms	0.47°	0.54°
GRAB Caustic	-	-	-	3.77 ms	0.87°	0.98°
WaveQ3D Direct	+0.06 dB	± 3.17 dB	97.0%	0.64 ms	0.21°	0.24°
WaveQ3D Caustic	+1.15 dB	± 4.07 dB	94.4%	3.97 ms	1.24°	1.40°

Differences in total propagation loss for the deep source geometry are illustrated in Fig. 31 and summarized in Table 8. In the region from 3000 to 3040 meters, the FFP has stronger oscillations than either the WaveQ3D or GRAB models. This can be attributed to surface reflected contribution that is stronger in the FFP result than in either of the Gaussian beam models. At all other ranges, the WaveQ3D and GRAB results were both a very close fit to FFP's total propagation loss.

A WaveQ3D anomaly was discovered during the deep source geometry testing. Errors

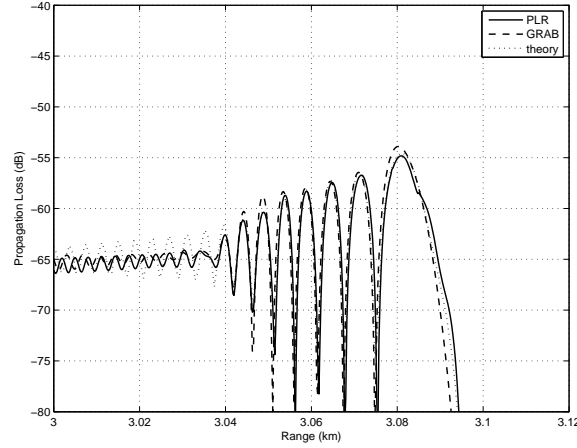


Fig. 31. Propagation loss for deep source.

Table 8. Total propagation loss for deep source.

Scenario	bias	deviation	r^2
GRAB	-0.95 dB	± 3.05 dB	95.4%
WaveQ3D	-0.22 dB	± 1.94 dB	92.8%
GRAB ≥ 3.04 km	-1.45 dB	± 3.70 dB	97.0%
WaveQ3D ≥ 3.04 km	-0.03 dB	± 2.20 dB	94.4%

in the total propagation loss within the shadow zone were frequently seen when the launch angles finer than 0.01 degrees were used. What we discovered was that at this spacing, the contribution in the shadow zone was the result of a summation of over 100 Gaussian beams for both the direct and caustic paths. Small errors in the calculation of cell width and cell distance to the target appear to accumulate when the total loss is the result of many weak contributions. For the individual eigenrays, this anomaly results in a slight broadening of the transmission loss decay tails. But, since the shape of the outer edge of the total propagation loss depends on destructive interference between the paths, these errors often resulted in imperfect cancellation, on the order of -70 dB, in the region between 3090 and 3105 meters. Although these problems may have been aggravated by the extreme environment, developers should use extra caution when using WaveQ3D with super-fine ray spacings.

5. Summary

This paper represents an important milestone the development of the WaveQ3D model. A suite of tests were developed to quantitatively compare the ray tracing, reflection, eigenray finding, and propagation loss elements of the model to analytic solutions. Hopefully, this approach will help other researchers evaluate the capability and limitations of the WaveQ3D model and provide a firm foundation to move forward with further testing.

This testing also led to the development of a few general guidelines for the use of the WaveQ3D model.

- Using a time step size as coarse as 100 ms seems to produce accurate results for most applications. However, this step size should be decreased to 10 ms for applications that need high accuracy at ranges less than 2 km. This is particularly true for applications that are interested in effects near the ocean surface, or directly below the source.
- The selection of launch angles can have a significant effect on propagation loss results. Like all models that are based on ray theory, WaveQ3D can miss features in the environment because of spatial under-sampling. Tangent spaced depression/elevation angles appear to improve WaveQ3D model performance for scenarios dominated by horizontal paths. Uniform spacing is suggested for applications that need high accuracy at ranges less than 2 km.
- The WaveQ3D model is designed to be computationally efficient when computing transmission loss for up to 100 targets, at multiple frequencies, in a fully 3-D environment. But because the WaveQ3D eigenray detection process is less efficient than an equivalent calculation in Cartesian coordinates, WaveQ3D can actually be much slower than other models when thousands of range/depth combinations are required. Applying the WaveQ3D model in 2-D environments is also not very efficient.

Acknowledgments

This paper was developed as part of Sean Reilly's PhD studies at the Ocean Engineering Department of the University of Rhode Island, under the direction of Dr. Gopu Potty and Dr. James Miller. This verification testing effort was funded by the High Fidelity Active Sonar Training (HiFAST) Project at the U.S. Office of Naval Research.

Appendix

A. Ray path derivation for concave ocean surface

The analytic solution for the direct-path eigenrays was derived from the laws of sines and cosines.

$$a^2 = r_1^2 + r_2^2 - 2r_1r_2\cos(\Delta\theta) , \quad (\text{A.1})$$

$$t_d = a/c_0 , \quad (\text{A.2})$$

$$\mu_{d,source} = -\arcsin\left(\frac{a^2 + r_1^2 - r_2^2}{2ar_1}\right) , \quad (\text{A.3})$$

$$\mu_{d,target} = \arcsin\left(\frac{a^2 + r_2^2 - r_1^2}{2ar_2}\right) , \quad (\text{A.4})$$

where t_d is the direct-path travel time from source to target; $\mu_{d,source}$ is the direct-path depression/elevation angle at source; and $\mu_{d,target}$ is the direct-path depression/elevation angle at target.

The analytic solution for the surface reflected solution also starts with the law of cosines.

$$\cos \beta = \frac{R^2 + b_1^2 - r_1^2}{2Rb_1} = \frac{R^2 + b_2^2 - r_2^2}{2Rb_2}. \quad (\text{A.5})$$

This can be reduced to a simpler form using

$$R^2 + b_n^2 - r_n^2 = R^2 + (R^2 + r_n^2 - 2Rr_n \cos(\Delta\theta_n)) - r_1^2 = 2R(R - r_n \cos(\Delta\theta_n)) \quad (\text{A.6})$$

to yield

$$\cos \beta = \frac{R - r_1 \cos(\Delta\theta_1)}{b_1} = \frac{R - r_2 \cos(\Delta\theta_2)}{b_2}. \quad (\text{A.7})$$

When this is combined with the law of sines

$$\sin \beta = \frac{r_1 \sin(\Delta\theta_1)}{b_1} = \frac{r_2 \sin(\Delta\theta_2)}{b_2}, \quad (\text{A.8})$$

it yields an analytic relationship between the source/target depths and the angles $(\Delta\theta_1, \Delta\theta_2)$ at which reflections occur

$$\frac{\cos \beta}{\sin \beta} = \frac{R/r_1 - \cos(\Delta\theta_1)}{\sin(\Delta\theta_1)} = \frac{R/r_2 - \cos(\Delta\theta_2)}{\sin(\Delta\theta_2)}, \quad (\text{A.9})$$

$$\frac{R}{r_1} \sin(\Delta\theta_2) - \sin(\Delta\theta_2) \cos(\Delta\theta_1) = \frac{R}{r_2} \sin(\Delta\theta_1) - \cos(\Delta\theta_2) \sin(\Delta\theta_1), \quad (\text{A.10})$$

$$r_1 \sin(\Delta\theta_1) - r_2 \sin(\Delta\theta_2) + \frac{r_1 r_2}{R} \sin(\Delta\theta_2 - \Delta\theta_1) = 0. \quad (\text{A.11})$$

The analytic solutions for the surface reflected path requires finding values of $\Delta\theta_1$ which solve the transcendental equation

$$r_1 \sin(\Delta\theta_1) - r_2 \sin(\Delta\theta - \Delta\theta_1) + \frac{r_1 r_2}{R} \sin(\Delta\theta - 2\Delta\theta_1) = 0. \quad (\text{A.12})$$

B. Tangent spaced depression/elevation angles

Because sonar detection ranges are often much longer than the depths of interest, there is frequently a need to emphasis propagation paths near the horizontal. The GRAB model¹⁷ manages this requirement by automatically adding rays in the depression/elevation directions needed to support caustics, surface ducts, and SOFAR channels. The WaveQ3D model currently does not support any such automatic ray adjustment; but it does support any ray spacing that is monotonically increasing.

Tangent spaced depression/elevation angles will be used frequently in the eigenray and propagation loss testing for WaveQ3D. As shown in the top panel of Fig. A.1, uniformly

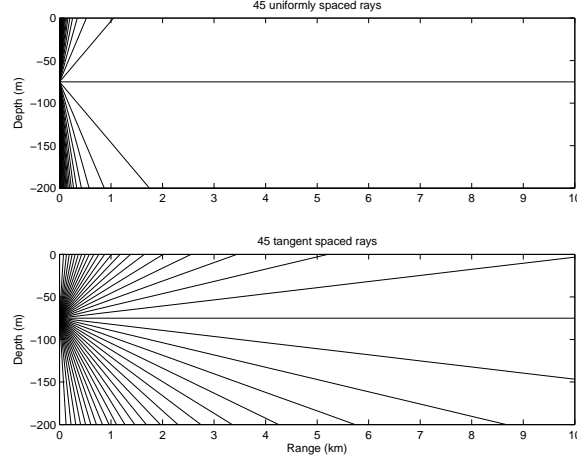


Fig. A.1. Tangent spaced beams.

spaced rays in an isovelocity environment severely under-sample the direct path contributions at ranges beyond a few kilometers. When the ray paths are initialized such that the tangents of the launch angles are uniformly spaced (bottom panel), the long range contributions are better supported. Of course, this improvement comes at the expense of short range contributions. But, that trade-off often matches the requirements of sonar simulations.

To generate a set of N tangent spaced beams $\mu[n]$, over the interval $[\mu_1, \mu_N]$, with the densest spacing at μ_c , WaveQ3D uses the following algorithm

$$a_1 = \arctan\left(\frac{\mu_1 - \mu_c}{\sigma}\right) \quad (\text{B.1})$$

$$a_N = \arctan\left(\frac{\mu_N - \mu_c}{\sigma}\right) \quad (\text{B.2})$$

$$x[n] = a_1 + \frac{a_N - a_1}{N - 1}n \quad \text{for } n = 0, 1, 2, \dots, N-1 \quad (\text{B.3})$$

$$\mu[n] = \mu_c + \sigma \tan(x[n]) \quad (\text{B.4})$$

where σ is an arbitrary scaling factor. WaveQ3D testing frequently uses 181 tangent spaced depression/elevation rays, from -90° to $+90^\circ$, with $\mu_c = 0^\circ$ and $\sigma = 6$. This combination of factors yields a ray fan with maximum resolution of about 0.1° and 85% of its rays in the $\pm 20^\circ$ range.

C. Propagation loss error statistics

We would like to define quantitative differences between modeled and analytic propagation losses in a way that illuminates the suitability of the model for real-time, sonar simula-

tion/stimulation systems. To that end, we define the following statistical measures

$$b[PL] = \frac{1}{N} \sum_{n=1}^N (PL_{model}[n] - PL_{theory}[n]) , \quad (C.1)$$

$$\psi^2[PL] = \frac{1}{N} \sum_{n=1}^N (PL_{model}[n] - PL_{theory}[n])^2 , \quad (C.2)$$

$$s[PL] = \sqrt{\psi^2[PL] - b^2[PL]} , \quad (C.3)$$

$$x[n] = PL_{theory}[n] - \frac{1}{N} \sum_{n'=1}^N (PL_{theory}[n'] , \quad (C.4)$$

$$y[n] = PL_{model}[n] - \frac{1}{N} \sum_{n'=1}^N (PL_{model}[n'] , \quad (C.5)$$

$$r^2[PL] = \frac{\left(\sum_{n=1}^N x[n]y[n] \right)^2}{\sum_{n=1}^N x^2[n] \sum_{n=1}^N y^2[n]} \times 100\% , \quad (C.6)$$

where $PL_{model}[n]$ and $PL_{theory}[n]$ are the samples in the model and theory in dB units; $b[PL]$ is the estimated bias between the model and the theory; $s[PL]$ is the estimated deviation between the model and the theory; and $r^2[PL]$ is the coefficient of determination between the model and the theory.

The active sonar equation can be expressed in the form

$$SE = FOM - 2PL , \quad (C.7)$$

$$FOM = SL + TS - NL + DI - DT , \quad (C.8)$$

where SE is the signal excess; PL is the propagation loss; FOM is the active figure of merit; SL is the source level; TS is the target strength; NL is the noise level; DI is the directivity index; and DT is the detection threshold.²⁰ If we assume that errors in the figure of merit are handled separately, then $2b[PL]$ and $s^2[PL]$ are estimates of signal excess bias and variance. The coefficient of determination, $r^2[PL]$, estimates how well the modeled signal excess' shape is correlated to an ideal solution.

References

1. S. M. Reilly, G. Potty, Sonar Propagation Modeling using Hybrid Gaussian Beams in Spherical/Time Coordinates, Department of Ocean Engineering, University of Rhode Island, January 2012.
2. T. Veldhuizen, "Expression Templates," C++ Report, Vol. 7 No. 5 June 1995, pp. 26-31
3. M. B. Chrissis, M. Konrad, S. Shurm, **CMMI Guidelines for Process Integration and Product Development**, Second Edition, (Addison-Wesley, New York, 2007).
4. Yakowitz and Szidarovszky, **An Introduction to Numerical Computation** (Macmillan Publishing, New York, 1986) pp. 306-311.
5. C. L. Pekeris, Accuracy of the Earth-Flattening Approximation in the Theory of Microwave Propagation, *Phys. Rev.* **70** (1943).
6. W. H. Munk, Sound channel in an exponentially stratified ocean, with application to SOFAR, *J. Acoust. Soc. Amer.* **55** (1974) pp. 220-226.
7. F. B. Jensen, W. A. Kuperman, M. B. Porter, and H. Schmidt, **Computational Ocean Acoustics**, *American Institute of Physics Press, New York* (1994).
8. M.B.Porter, The KRAKEN Normal Mode Program (DRAFT), A Deep Water Problem: the Munk Profile (1997) <http://oalib.hlsresearch.com/Modes/AcousticsToolbox/manual.html/node8.html>.
9. V. Cerveny, **Seismic Ray Theory**, (Cambridge University Press, New York, 2001), pp.174-178.
10. L.F. Shampine, Vectorized Adaptive Quadrature in MATLAB, *J. Comput. Appl. Math.* **70** (2008).
11. E. Williams, Aviation Formulary V1.46, <http://williams.best.vwh.net/avform.htm>, 2011
12. M. A. Pedersen, D. F. Gordon, Normal-Mode and Ray Theory Applied to Underwater Acoustic conditions of Extreme Downward Refraction, *J. Acoust. Soc. Amer.* **51** (1972) 323.
13. M. B. Porter, H. P. Buckner, Gaussian beam tracing for computing ocean acoustic fields, *J. Acoust. Soc. Amer.* **93** (1987) 1349.
14. H. Weinberg, R. E. Keenan, Gaussian ray bundles for modeling high-frequency propagation loss under shallow-water conditions, *J. Acoust. Soc. Amer.* **100** (1996) 1421.
15. ETOPO1v2 Global Gridded 2-minute Database, National Geophysical Data Center, National Oceanic and Atmospheric Administration, U.S. Dept. of Commerce, <http://www.ngdc.noaa.gov/mgg/global/ETOPO1.html>.
16. F. Sturm, S. Ivansson, Y. M. Jiang, N. R. Chapman, Numerical investigation of out-of-plane sound propagation in a shallow water experiment, *J. Acoust. Soc. Amer.* **124** (2008) pp. 341-346.
17. Software Requirements Specification/Software Design Description and Software Test Description for the Oceanographic and Atmospheric Master Library Navy Standard Comprehensive Acoustic System Simulation Model Version 4.2A, *Naval Meteorology and Oceanography Command Report OAML-SRS-SDD-STD-83D* (2008).
18. F. R. DiNapoli, R. L. Deavenport, Theoretical and numerical Green's function field solution in a plane multilayered medium, *J. Acoust. Soc. Amer.* **67** (1980).
19. L. M. Brekhovskikh, *Waves in Layered Media* (Academic Press Inc., New York, 1980), 2nd Edition, Section 54.
20. R. J. Urick, **Principles of underwater sound, 3rd edition**, *McGraw-Hill, New York* (1983).